catalysts

MDPI

Review

ZrO_2-Based Photocatalysts for Wastewater Treatment: From Novel Modification Strategies to Mechanistic Insights

Vandna Rani [1], Amit Sharma [1], Abhinandan Kumar [1], Pardeep Singh [1], Sourbh Thakur [2], Archana Singh [3], Quyet Van Le [4], Van Huy Nguyen [5] and Pankaj Raizada [1,*]

1 School of Advanced Chemical Sciences, Faculty of Basic Sciences, Shoolini University, Solan 173229, HP, India
2 Department of Organic Chemistry, Bioorganic Chemistry and Biotechnology, Silesian University of Technology, B. Krzywoustego 4, 44-100 Gliwice, Poland
3 Advanced Materials and Processes Research Institute, Hoshangabad Road, Bhopal 462026, MP, India
4 Department of Materials Science and Engineering, Korea University, 145, Anam-ro Seongbuk Gu, Seoul 02841, Korea
5 Faculty of Allied Health Sciences, Chettinad Academy of Research and Education (CARE), Kelambakkam, Chennai 630102, TN, India
* Correspondence: pankajchem1@gmail.com

Abstract: Zirconium dioxide (ZrO_2) has garnered substantial research interest in the field of photocatalytic water treatment due to its appealing properties, such as thermal stability, considerable physical strength, and strong chemical resistance. However, the wide bandgap energy endorses less photoabsorption and rapid charge carrier recombination kinetics, thus restricting the photoactivity of ZrO_2. Previously, vast research efforts have been made to improve the photoefficacy of ZrO_2, and hence it is worth exploring the potential strategic modifications responsible for incremented photocatalytic efficiency. In this regard, the present review article emphasizes the optical, structural, and electronic features of ZrO_2, which makes it an interesting photocatalytic material. The exceptional modification strategies that help to modulate the crystal structure, morphology, bandgap energy, and charge carrier kinetics are primarily discussed. The potential synthetic routes involving bottom-up and top-down methods are also outlined for understanding the rationale for incorporating these techniques. Moreover, the photocatalytic performance evaluation was done by investigating the photodegradation kinetics of various organic and inorganic pollutants degradation by ZrO_2. Conclusively, in light of research advances involving ZrO_2 photocatalyst, this review article may expedite further investigation for enhancing the large-scale photocatalytic applications for environmental and energy concerns.

Keywords: ZrO_2; organic and inorganic pollutant degradation; strategic modifications; photodegradation

check for updates

Citation: Rani, V.; Sharma, A.; Kumar, A.; Singh, P.; Thakur, S.; Singh, A.; Le, Q.V.; Nguyen, V.H.; Raizada, P. ZrO_2-Based Photocatalysts for Wastewater Treatment: From Novel Modification Strategies to Mechanistic Insights. *Catalysts* **2022**, *12*, 1418. https://doi.org/10.3390/catal12111418

Academic Editors: Hideyuki Katsumata and Anna Kubacka

Received: 22 August 2022
Accepted: 9 November 2022
Published: 11 November 2022

1. Introduction

The past several decades have witnessed a tremendous rise in industrialization, agrochemical processes, and excessive exploitation of non-renewable resources, resulting in extreme deterioration of water resources [1,2]. Owing to the exclusion of these multifarious exactor pollutants from contaminated water and to abate their dangerous consequences on the ecosystem, several conventional methods for eliminating organic and inorganic pollutants have been used, including biodegradation, adsorption, coagulation, flocculation, chlorination, reverse osmosis, chemical precipitation, ion exchange, etc. [3,4]. However, these are not proven to be effective enough to eradicate these recalcitrant compounds because of their unreasonable resistance and less biodegradability [5–7]. Further, these approaches have several drawbacks, including high maintenance costs, significant sludge formation, limited scale application, excessive energy consumption, long processing period, and incomplete degradation of persistent pollutants [8–10]. Currently, numerous research efforts have addressed advanced oxidation processes (AOPs) because of their ability to

generate reactive oxidative species for the effective and rapid degradation of these toxic industrial effluents to safe biodegradable mineralized salts, CO_2, and H_2O [11–13]. This special class of oxidation methods is environmentally benign, sustainable, and operates at feasible temperature and atmospheric pressure [14–16].

Photocatalysis is an interesting AOP that has been given substantial attention due to its features like effective degradation of pollutants without generating harmful by-products, cost-effectiveness, high efficiency, and the ability to operate under the illumination of solar light [17,18]. Heterogeneous photocatalysis is a photo redox reaction that proceeds with the harnessing of light by a semiconductor, specifically including the generation of e^-/h^+ pairs, capturing of charges at the surface, and inter-interface charge transfer [19,20]. Typically, in photocatalysis, the initiating event is the photoexcitation of electron-hole pairs (EHP) via absorption of the radiation within the bandgap energy. The photoinduced electrons and holes reduce O_2 into the superoxide radical $\bullet O_2^-$ (−0.33 V vs. SHE at pH = 7) and oxidize H_2O and OH^- into •OH (2.8 V vs. SCE at pH = 0) radicals for photo-oxidation reactions, respectively. [14]. The hydroxyl radicals have a short life span due to a single unpaired electron which readily attacks a series of organic wastes (e.g., dyes, insecticides, pesticides, antibiotics, etc.) that are often hard to degrade, showing rate constants typically in the order of 10^6–10^9 $M^{-1}s^{-1}$ [17,21].

Water treatment by photocatalysis using inorganic semiconductors like TiO_2, SnO_2, CuO, and ZnO, has been vastly explored owing to its non-toxic nature, optical properties, and reasonable cost [22]. For instance, Fujishima and Honda, in 1972, reported the photoelectrolysis of water using TiO_2, because of its cost-effectiveness, chemical and photochemical stability, and non-toxic nature [23]. Currently, ZrO_2 as broad bandgap (3.25–5.1 eV) semiconductor has been widely explored due to the presence of a large number of oxygen vacancies on the surface, significant ion exchange ability and physiochemical stability [23]. However, ZrO_2 possesses a high value of the dielectric constant, tensile strength, melting and boiling point, however its wide band gap and low separation rate of photogenerated electron and hole hinder the wide-scale applications [24]. To overcome this, various enhancement strategies like doping, heterojunction formation incorporation of cocatalysts, etc., have been potentially explored. For instance, Co doped ZrO_2 synthesized by facile-chemical precipitation showed greater degrading activity against MB dye when exposed to visible light due to the improved dielectric properties [25]. However, coupling ZrO_2 with narrow band semiconductors like MoS_2, TiO_2, and g-C_3N_4 also retards the photocarrier reassembly and augments its photocatalytic performance [26]. The optical properties of ZrO_2 can be enhanced by introducing new electronic states by doping with rare earth metals. For example, the introduction of Ce (IV) ions in ZrO_2 enhanced the photoresponse through the formation of midgap states and the Ce 4f empty states acted as a electron transfer bridge between VB and CB of ZrO_2 by low energy photons [27].

Recent research has manifested that zirconia-based materials show high redox abilities, large surface area, and low thermal conductivity in photocatalytic processes. In this regard, Aldeen et al. comprehensively explored the altered ZrO_2 based photocatalysts for organic pollutant degradation [24]. However, the typical insights of inorganic pollutant degradation, specifically the heavy metal ions present in waste water, are missing. Additionally, the importance of generating oxygen vacancies (OVs) in ZrO_2 for the synergistic improvement in opto-electronic properties still needs further comprehension. Hence, the present review article highlights the features of ZrO_2 semiconducting material for the photocatalytic removal of organic as well as inorganic pollutants present in wastewater. Starting from the optimal crystal structure of ZrO_2, various phases and the subsequent photocatalytic features are comprehensively reviewed. Significant methods to circumvent the inherent drawbacks of the bare ZrO_2 photocatalyst have been inclusively illustrated using different methods such as doping, heterojunction formation, morphology, and structural modulation along with the formation of OVs. After this, the review introduces facile synthesis routes involving bottom-up (solvothermal, Morphology control, and doping) and top-down methods (ultrasonication and chemical reduction) to design ZrO_2-based photocatalytic

materials. Then, in order to highlight the advancement of ZrO_2 as a photocatalyst, the mechanistic insights of wastewater treatment via photocatalysis of organic and inorganic pollutants have been broadly reviewed. Lastly, the review summarizes various challenges in the field with a broad perspective to scale up the photocatalytic applications of ZrO_2 with the purpose of solving the burgeoning environmental crisis in the world.

2. ZrO_2 as Photocatalyst

ZrO_2 is an n-type semiconducting material that possesses a bandgap energy of 5.0 eV, which facilitates its application in the heterogeneous catalysis [28,29]. Moreover, the tremendous properties of ZrO_2, like thermal stability, high strength, strong chemical resistance, ductility, and low thermal conductivity makes it an alluring photocatalytic material [25]. Consequently, ZrO_2 has been explored for different applications, such as oxygen sensors, power device electrolytes, colors for sharpened sunlight-based cells, the photocatalytic parting of water for hydrogen creation, the particular amalgamation of natural mixtures, air refinement, and photocatalytic abatement of organic and inorganic pollutants present in wastewater [30]. Certain other features of ZrO_2, which endorse its usage as photocatalytic material, are described as follows:

- ZrO_2 is a transition metal oxide and a prominent candidate for photocatalysis owing to its high refractive index, high corrosion resistance, and good photochemical stability, as well as optical absorption ability [31,32].
- ZrO_2 is rich in OVs, which exist on the surface or in the lattice's interstitial sites, which further promotes the optoelectronic properties of ZrO_2 leading to boosted light harvesting ability and superior isolation of photocarriers [22].
- The optical characteristics of ZrO_2 are modified by the introduction of midgap states in the elemental doping, resulting in optimal visible light responsive photocatalyst [22]. By doping with ZrO_2, ions diffuse throughout the lattice at interstitial sites, resulting in a new valance band maximum (VBM) or conduction band minimum (CBM), which narrows the optical bandgap of ZrO_2 [33].

2.1. Crystal Structure

The three major polymorphs of ZrO_2, namely monoclinic, tetragonal, and cubic crystal structures are depicted in Figure 1. At ambient temperature, the monoclinic stage remains constant, but when heated to 1170 °C, it transforms to the tetragonal ZrO_2 and further to cubic ZrO_2 by increasing the temperature up to 2370 °C. The transformation is reversible when the temperature is lowered; the shift from tetragonal to monoclinic occurs at a lower temperature (around 950 °C) [34]. Tetragonal ZrO_2 is formed by the elongation of any of the three equal axes of cubic fluorite-type structure and the relocation of oxygen anions from their characteristic places in the same direction [35].

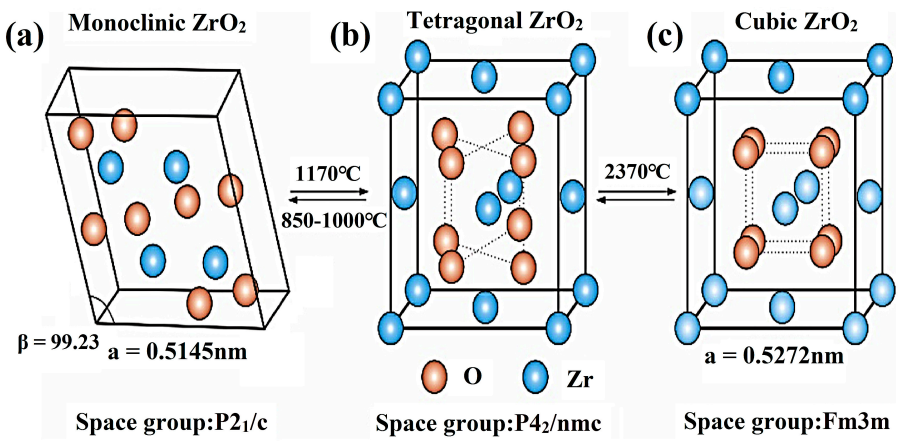

Figure 1. Schematic representation of crystal structures of ZrO_2 (**a**) monoclinic ZrO_2, (**b**) tetragonal ZrO_2, and (**c**) cubic ZrO_2, reprinted with permission from Elsevier (License NO. 5332051438018) [34].

The main features of monoclinic ZrO_2 involve sevenfold coordination of the Zr-atom and alteration of fluorite layers possessing OII ions in the tetrahedral coordination with triangular coordinated layers containing OI. Additionally, the nearest Zr-O distance is observed to be 3.77 Å, which signifies the coordination number to be seven (Figure 1a). The Zr-OII bond length in the OII coordinated tetrahedron varies from 2.16 to 2.26 Å, while the central bond angles at OI range from 100 to 132°. The Zr-OI bond length in the OI coordinated triangle is 2.04 Å, 2.10 Å, and 2.15 Å with 2.10 Å as an average angle, while the central angles at OI are 106°, 109°, and 145° [36]. The surface site of m-ZrO_2 consists of oxygen vacancies, unsaturated surface hydroxyl groups (Zr-O pairs), and Lewis's acid sites (Zr^{3+}, Zr^{4+}). In comparison to other phases, monoclinic-ZrO_2 has a less symmetrical lattice structure, making it a more adaptable surface for catalytic activity [37].

In the case of tetragonal ZrO_2, the Zr-atoms are surrounded by oxygen atoms (eight), four of which are in a flattened tetrahedron at a distance of 2.065 Å and the remaining four at a distance of 2.455 Å in an extended tetrahedron (Figure 1b). Each oxygen atom has two oxygen neighbors at 2.635 Å and four at 2.655 Å, which are connected to two Zr-atoms at 2.065 Å, and two more Zr-atoms at 2.455 Å [38]. The tetragonal phase is more active than the other two phases due to the presence of defects and its stable nature. t-ZrO_2 is excellent for photocatalytic reactions because of its antioxidant activity for free radical trapping, high redox ability, chemical and optical stability, and environmental affinity [25]. The cubic phase is thermally stable above 2300 °C, so it is rarely produced at low temperatures (Figure 1c). Yttrium doping was used to successfully construct cubic ZrO2 structures with abundant OVs, resulting in cubic yttria-stabilized zirconia [39,40].

2.2. Bandgap Formation

Compared to the normal hydrogen electrode (NHE), ZrO_2 possesses a strong reduction ability due to its comparatively high CBM, which is roughly 2.1 V less than the $O_2/\bullet O_2^-$ redox potential, yet its VBM is more positive (approximately 0.7 V) than the $H_2O/\bullet OH$ = 2.72 V (vs. NHE) potential [28,41]. The VB edge of ZrO_2 fundamentally arises from the O 2p orbitals, whereas the CB edge is overwhelmed by the 4d orbitals of Zr. The VB potential is 2.77 V higher than the required potential for water oxidation, whereas the CB edge is 1.0 V lower in potential than the hydrogen reduction level [42]. The lowest CB potential is ca. 1.0 V (vs. NHE, pH 0), which is considerably lower than the TiO_2 anatase (0.1 V) potential, and the highest VB potential is ca. +4.0 V, which is superior to TiO_2 (+3.1 V), suggesting that the band potentials of ZrO_2 are highly appropriate for various photocatalytic applications [27].

2.3. Opto-Electronic Properties

Density Functional Theory (DFT) studies can anticipate the characteristics of a material with less inconsistency and estimate bandgap due to the capability to detect quantum mechanical features of atoms, sub-atomic constituents, and inexact depiction of electronic interactions through generalized density approximation (GGA) and local density approximation (LDA), respectively. In the DFT analysis, the unit-cell structures of the oxide are optimized and determined by the lattice parameters for understanding the structural characteristics. Through DFT, it is found that ZrO_2 exhibits twelve ionic structures containing four formula units in ZrO_2, with seven O atoms surrounding the cation and two oxygen locations OI and OII in Wyckoff points. Each unit cell is thought to be made up of three distinct ions due to the varying atomic locations of the oxygen atom. An average bond length of 2.86 Å and 3.58 Å for Zr-O and Zr-Zr, respectively, was observed [43]. The structure of pure ZrO_2 is found to be cubic, which belongs to the space group "Fm3m" (N 225) with zirconium occupied position at (0, 0, 0), and oxygen atoms at (1/4, 1/4, 1/4) and (3/4, 3/4, 3/4), respectively (Figure 2a) [32].

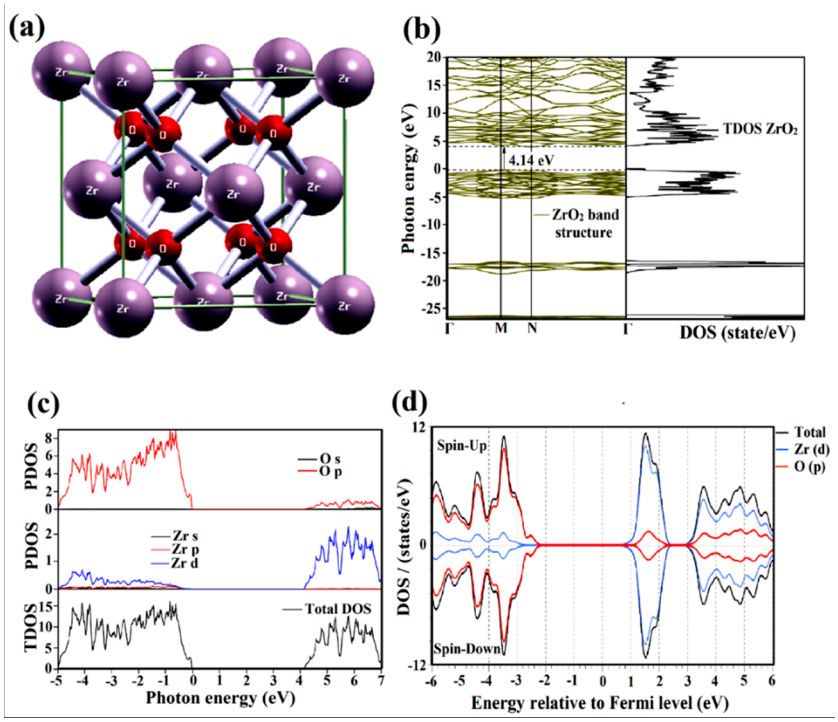

Figure 2. (**a**) Systematic diagram of pure ZrO_2 by Xcrysden package, reprinted with permission from Elsevier (License NO. 5332600596921) [32] (**b**) band structure and total density of state of ZrO_2. (**c**) Partial density of states (PDOS) and total density of states (TDOS) of ZrO_2, (**d**) PDOS and TDOS of pure ZrO_2, reprinted with permission from Elsevier (License NO. 5332600898565) [43].

Interestingly, the DFT calculation studies are further helpful to explore the intricate electronic structures of ZrO_2. The electrical levels of a crystal structure are presented by the bandgap positioning estimated through the Bloch vector (k) and the band index (n). When Fermi energy is set to the zero level, ZrO_2 showed an indirect band gap, with the placement of CBM and VBM at M and N, respectively (Figure 2b). Furthermore, the density of states (DOS) indicates the number of unoccupied levels accessible for the electron to be occupied at a certain energy level. The total density of state (TDOS) and partial density of state (PDOS) charts can be used to show the contribution of distinct atoms. In the case of ZrO_2, four different bands are present with the appearance of a lowest band around 27 eV. The next energy band starts from 19 to 16.5 eV with the upper VB positioning in between 5.3–0 eV and the CB at 4.14 eV. In the lowest VB states, Zr 3p states contribute the most while O 2 s state participates in the lower VB formation. In the VB below the Fermi level, O 2p states are the dominant states, with minor assistance from Zr 4d and 5 s hybridized orbitals. The Zr 4d and O 2p orbitals dominate the formation of CB as shown in Figure 2c [43]. The partial DOS (Figure 2d) further represents the characteristics of ionic bonding between the O 2p and Zr 4d orbitals placed below and above the Fermi energy level, respectively.

3. Modification Strategies

ZrO_2 is a potential photocatalyst due to its advantages of appropriate redox potentials, exceptional oxygen storage capacity, high thermal and chemical strength, etc. However, the limitations of smaller surface area, restricted visible light captivation, and speedy charge carrier recombination rate reduced the efficiency of the ZrO_2 photocatalyst. To overcome these drawbacks, various modification strategies have been incorporated so far, such as doping, heterojunction formation, morphology and structural modulation, and formation of OVs. These strategies are reported to increment the photocatalytic activity of the ZrO_2 photocatalyst, as discussed below.

3.1. Morphology and Structural Modulation

Modulation in the morphology and structure is an effective means to enhance the photocatalytic performance of photocatalysts as it can increase the specific area, amend the surface-active sites for photocatalytic reactions, facilitate the mass transportation and light harvesting along with accelerated charge migration and suppressed charge recombination [44]. Generally, factors like pH, temperature, reducing agents, etc., dominantly influence the morphology of photocatalysts and in turn affect the photocatalytic performance. However, the morphology of ZrO_2 photocatalyst can also be modified by varying the dopant concentration. In particular, the porosity of ZrO_2 nanoparticles can be enhanced by varying the dopant concentration. For instance, the variation in the morphology of ZrO_2 photocatalyst was observed by varying the concentration of Mg^{2+} ion dopant from 0.1 to 5 mol% [45]. From scanning electron microscope (SEM) results (Figure 3a), the hollow sphere structure of the ZrO_2 photocatalyst was observed with a large number of cracks at the surface indicating a highly porous nature. The unique interaction between Zr^{4+} and Mg^{2+} ions resulted in a complex polysaccharides structure with strong bindings. Furthermore, the increase in the Mg^{2+} ion concentration in ZrO_2 photocatalyst leading to increased light absorption capability due to the development of mid-gap states. Thus, Mg doping in ZrO_2 could facilitate the enhancement in light harvesting, efficient inhibition in the reassembly of charge carriers, and incremented specific surface area corresponding to improved photocatalytic performance.

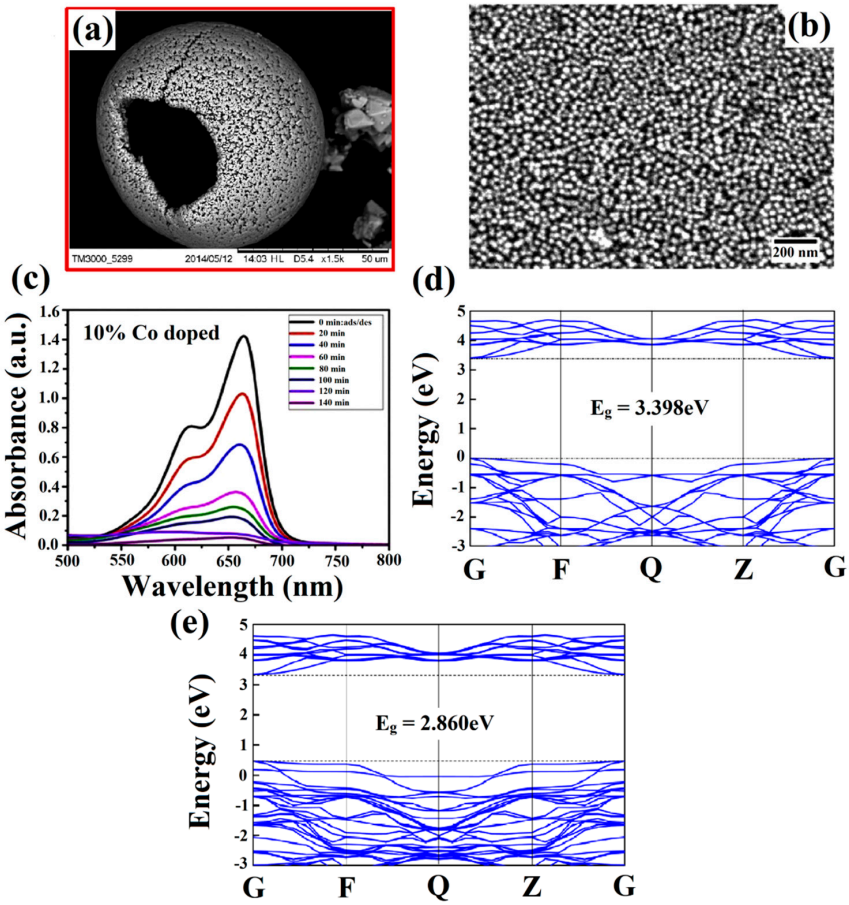

Figure 3. SEM images of (**a**) ZrO_2: Mg^{2+} 2 mol%, reprinted with permission from Elsevier (License NO. 5332611047818) [45], (**b**) Co-doped ZrO_2, (**c**) photodegradation of MB of 10% by Co doped ZrO_2 in visible light exposure, reprinted with permission from Elsevier (License NO. 5332971176132) [25], (**d**) band structure of pure ZrO_2, and (**e**) $ZrO_{2-x}N_x$ [46].

Ahmed et al. also studied the variation in morphology of the ZrO_2 photocatalyst after doping with cobalt ions [25]. The SEM results (Figure 3b) reveal that both the un-doped and Co-doped ZrO_2 photocatalyst presented spherical structures having identical size and showed ultrafine morphology. Thus, the parameters like shape and size intensities were influenced by the presence of defects that leads to the lowering of electron-hole pairs reassembly which contributed to boosted photocatalytic activity. In a different study, the cube-like or star-like morphology of the ZrO_2 colloidal nanocrystal clusters (CNCs) was also observed by varying the reaction conditions [47]. The occurrence of Cl^- ions in the hydrothermal process resulted in the establishment of cube-like ZrO_2 CNCs with a rough surface and increased particle size from 74 to 170 nm by incrementing the reaction time (six to ten hours). Furthermore, the morphology of ZrO_2 CNCs changed to star-like structures by the combined action of both Cl^- and Na^+ ions in the hydrothermal process due to its highly crystalline nature and systematic aggregation of nanocrystals. Additionally, the clustering of ZrO_2 nanocrystals takes place at high temperatures (150–240 °C), which leads to the formation of a cube-like morphology.

3.2. Bandgap Tuning via Doping

The band gap of semiconductors can be modulated by elemental doping, which triggers the creation of the allowed defective electronic levels within the bandgap energy and promotes the electronic excitation with lesser energy. To date, doping of ZrO_2 photocatalyst has been performed with noble metals [48], non-metals [49], and transition elements to adjust its band gap, amend the photoactivity, and inhibit the electron-hole pairs recombination rate [20]. For instance, $Co^{2+/3+}$ ions with radii 0.74 Å comparable to Zr^{4+} (0.80 Å) are reported to be an appropriate dopant as it can modify the optical properties and dielectric characteristics of ZrO_2 photocatalyst along with a reinforced charge separation rate leading to higher photocatalytic activity [25]. With the varied dopant concentration of Co from 3%, 5%, 7%, to 10%, the band gap energy of ZrO_2 photocatalyst changed from 3.7 eV to 2.74, 2.40, 2.23, and 2.12 eV, respectively (Figure 3c), due to the presence of OVs and dislocation defects. However, the optimal Co-doping concentration was found to be 10% in ZrO_2 photocatalyst for the highest degradation of 96.5% of methylene blue (MB). Other than the transition metal dopant, boron doping into oxygen vacancy-rich ZrO_2 (B@ZrO_2-OV) reportedly resulted in more impurity electronic levels, which significantly reduced the band gap value and boosted the capability of ZrO_2 to harvest light in the visible region [28]. Consequently, the B@ZrO_2-OV photocatalyst exhibited prompted photocatalytic performance by degrading 87% of RhB and 71% of the colorless phenol owing to enhanced photon harvesting capability.

The DFT study was used to analyze the decrement in bandgap energy of N doped ZrO_2 photocatalyst that further facilitated the separation of photocarriers. The DFT calculation was helpful in analyzing the effect of N-doping in the ZrO_2 photocatalyst with its subsequent impact on the band structure and electronic density of states in N-doped ZrO_2 ($ZrO_{2-x}N_x$, x = 0.125) [46]. The results revealed that the band gap of ZrO_2 photocatalyst narrowed down from 5.0 to 2.860 eV by doping with N atoms, as shown in Figure 3d,e. Furthermore, the VBM increased from 0 to 0.473 V, while the CBM decreased from 3.398 to 3.333 V. Consequently, the introduction of N-atoms in a substitutional mode of ZrO_2 photocatalyst resulted in the narrowed bandgap and extension of visible light absorptivity giving rise to enhanced photocatalytic degradation of formaldehyde (HCHO) into CO_2 under the exposure of visible light for 50 min.

Doping with Au has also facilitated the reduction in bandgap energy of ZrO_2 reduced from 5.72 to 5.40 eV [50]. With the increase in Au concentration, interactions occur between charge carriers and ionized impurities leading to a decreased band gap and photoluminescence (PL) intensity of ZrO_2 photocatalyst. Hence, doping is an effective way to boost the photoactivity of the ZrO_2 photocatalyst with noble metals, non-metals, and transition metals by tuning the bandgap energy to some extent by varying the concentration of impurity atoms.

3.3. Heterojunction Formation

Heterojunction formation is one of the most important ways to achieve better photocatalytic activity by reducing the high charge recombination rate, less visible-light absorption, and low electron utilization ratio [51]. ZrO_2 has reportedly formed type-I heterostructure systems for water treatment applications. For instance, the formation of a type-I heterojunction for modulating the photocatalytic efficiency of ZrO_2/ZnO heterojunction was efficiently reported [52]. With the formation of optimized ZrO_2/ZnO (1:2) heterojunction, the bandgap energy of the nanocomposite was decreased from 5.3 to 3.2 eV. Additionally, the ZrO_2/ZnO (1:2) heterojunction exhibited 93% photocatalytic degradation of Acid orange 8 (AO 8) under UV light illumination. In a different study, the photo-absorption ability of ZrO_2 photocatalyst was reportedly enhanced when coupled with Polypyrrole (PPy) in the type-II mechanistic mode [53]. The decreased eh^+ recombination rate and enhanced isolation of charge carriers were accredited to the type-II system with reduced bandgap energy from 3.26 to 2.45 eV. Moreover, the photocatalytic performance of the ZrO_2/PPy system was assessed by degrading Reactive Black 31 (RB 31; 77%) and 4-chlorophenol (4-CP; 98%) under the exposure of visible light for 60 min. The synergic effect between the ZrO_2 and PPy photocatalysts after heterostructure formation improved the charge carrier kinetics and provided sufficient carriers at the surface for photoredox reactions. While ZrO_2-based type-I and type-II heterojunctions have shown considerable photocatalytic performance, the accumulation of photocarriers on one photocatalyst only and the electrostatic forces of repulsion between charge carriers along with the decreased redox potential in type-II system hampers the overall photocatalytic performance [54]. Thus, the formation of the Z-scheme photocatalytic system is considered to be a prominent approach that has been vastly opted to expedite the photocatalysis process.

For example, the photoactivity of g-C_3N_4/ZrO_{2-x} Z-scheme heterojunction was analyzed for wastewater treatment [55]. The report illustrated that, due to the involvement of the Z-scheme charge transference, the g-C_3N_4/ZrO_{2-x} system exhibited extended visible light irradiation and enhanced separation of charge carriers. Additionally, the presence of abundant, spatially separated e- facilitated the formation of $\bullet O_2^-$ species, which primarily participated in the degradation process. Consequently, g-C_3N_4/ZrO_{2-x} system showed 90.6% tetracycline hydrochloride (TC-H) degradation under 1 h exposure to visible light (Figure 4a). Similarly, the photodegradation of Congo Red (CR) dye was reported by Hao et al. by utilizing the Ag/CeO_2-ZrO_2 nanocomposite [56]. The formation of three-dimensionally ordered macroporous Ag/CeO_2-ZrO_2 composite enabled the absorption of reactive molecules on the surface of photocatalysts, which reduced the recombination probability of charge carriers leading to enhanced photocatalytic performance.

Interestingly, the arrangement of the S-scheme heterojunction is quite similar to Type-II but it follows a completely different charge transfer mechanism [57]. Typically, the photoexcited e^- and h^+ are accumulated on the CB of reduction photocatalyst (RP) and VB of oxidation photocatalyst (OP), respectively, which corresponds to a strong redox potential. The remaining (unutilized) photocarriers are eliminated through recombination, leading to better photocatalytic reactions. For instance, the formation of the S-scheme g-C_3N_4/ZrO_2 heterojunction was achieved via a simple calcination method for improved photocatalytic performance [26]. The g-C_3N_4/ZrO_2 S-scheme heterojunction inhibited the recombination rate of photocarriers due to a sufficiently exposed large specific surface area with abundant active sites. Moreover, the optimized 15% g-C_3N_4/ZrO_2 heterojunction exhibited excellent photocatalytic performance by degrading 82% RhB, 50% methyl orange (MO), and 98% acid orange II (AO II) under visible light irradiation for 150 min (Figure 4b).

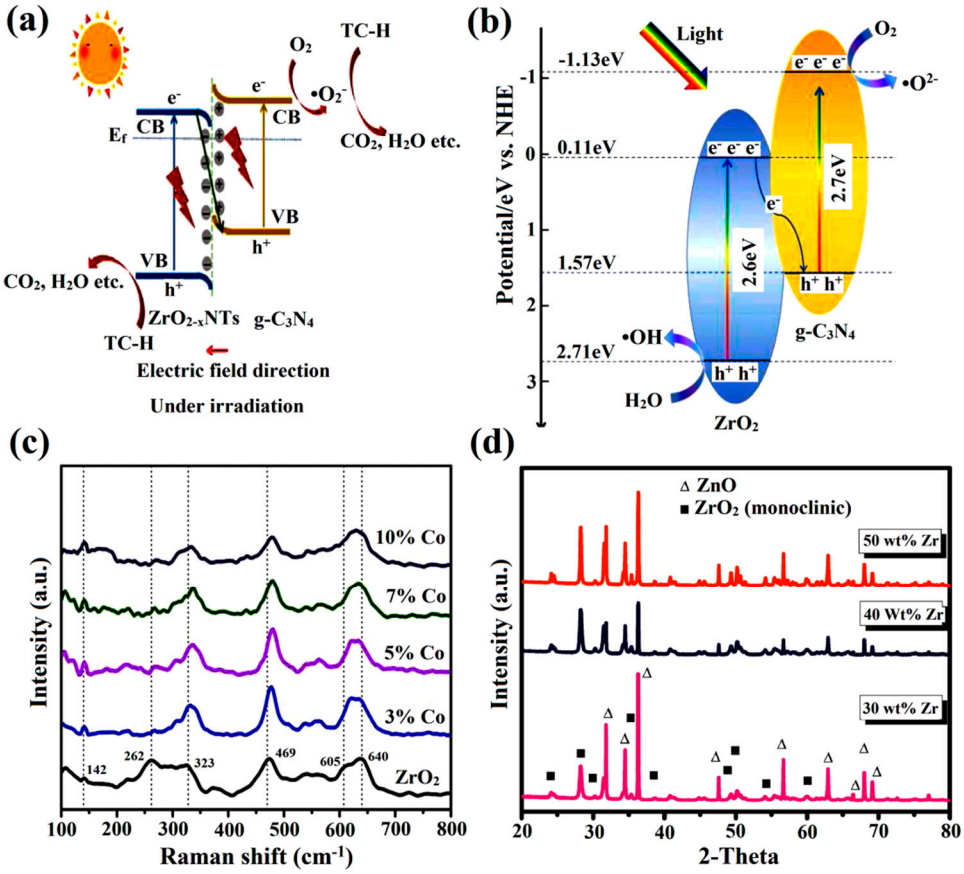

Figure 4. (**a**) Systematic representation of TC-H degradation in g-C_3N_4/ZrO_{2-x} NTs, reprinted with permission from Elsevier (License NO. 5332980412880) [55]. (**b**) The plausible photocatalytic mechanism of g-C_3N_4/ZrO_2 heterostructure, reproduced with permission from Elsevier (License NO. 5332980598897) [26]. (**c**) Raman spectra of pure ZrO_2 and Co doped ZrO_2 NPs, reprinted with permission from Elsevier (License NO. 5332971176132) [25]. (**d**) XRD analysis of pure ZnO and Zr-doped ZnO, reprinted with permission from Elsevier (License NO. 5332980782041) [22].

3.4. Generation of Oxygen Vacancies

The introduction of OVs in the ZrO_2 photocatalyst is a useful strategy to increase the absorption range in the visible light region and to promote the adsorption affinity leading to enhanced photocatalytic degradation efficacy. The formation of vacancies in ZrO_2 crystal acts as a trapping site for one or more electrons, which gives rise to F-centers with the local states in the crystal energy gap and produces the new energy band near the Fermi level [58]. The determination of OVs and surface defects can be done with the help of PL intensity, X-ray photoelectron spectroscopy (XPS), and X-ray diffraction (XRD) pattern. Over the past few years, various works have reported the successful generation and identification of OVs in the ZrO_2 photocatalyst.

For instance, OVs in ZrO_2 were created by depositing Co on its surface [25]. The XRD pattern identified the presence of OVs due to the distinct ionic radii of Zr and Co ions. The slight shift in the peak position intensity of Raman spectra (Figure 4c) and decreased the band gap energy of Co-ZrO_2 occurred by the presence of OVs and surface defects. Furthermore, the OVs trapped the photogenerated e- leading to the formation of F-centers in the crystal structure of ZrO_2, which inhibit the charge carrier's reassembly and amend the photocatalytic performance. Wahba et al. studied the formation of OVs in the Zr-doped ZrO_2/ZnO heterojunction through experimental and simulation studies [22]. The XRD pattern revealed that, with the increasing concentration of Zr from 30 to 50 wt%, two diffraction peaks corresponding to monoclinic ZrO_2 and wurtzite hexagonal ZnO were obtained as delineated in Figure 4d. Additionally, the Zr^{4+} ions were replaced by

Zn^{2+} ions, which induced the OVs in the crystal structure for trapping charge carriers and increasing their separation. XPS analysis can also be employed to evaluate the presence of OVs in ZrO_2 photocatalysts. For instance, Reddy et al. reported the formation of OVs in Ni-doped ZrO_2 by analyzing the XPS spectra of O 1 s [59]. In detail, the XPS study showed three types of OVs on the ZrO_2 surface that is neutral, singly charged and doubly charged oxygen vacancy with different binding energies. The binding energy 530.7 eV, and 532.1 eV corresponded to singly and doubly charged OVs in ZrO_2 photocatalyst, respectively.

From the above study, it is evident that the modification strategies are significantly effective in incrementing the photocatalytic performance of the ZrO_2 photocatalyst. The change in morphology and optoelectronic structure of ZrO_2 leads to enhanced visible light absorption and superior charge isolation. Doping with suitable dopants and the formation of ZrO_2-based heterojunctions resulted in narrowed bandgap energy and improved charge carrier kinetics enabling their effectiveness in photocatalytic performance. Additionally, the presence of OVs not only acts as trapping sites for photoinduced charge carriers, but also renders defective states in between the bandgap energy which synergistically enhances the photoactivity of ZrO_2 nanomaterials.

4. Synthesis Methods

ZrO_2 photocatalysts having different morphologies, sizes, and compositions have been designed by various bottom-up and top-down strategies for efficient photocatalytic activity. Different advantages and challenges in the fabrication of ZrO_2 using distinct synthesis methods are discussed as follows.

4.1. Bottom-Up Strategies

4.1.1. Hydrothermal/Solvothermal Method

The hydrothermal/solvothermal strategy is a synthesis method for the preparation of the ZrO_2 photocatalyst, which involves a sealed vessel with water or any organic solvent as a reaction medium [60]. The crystallization of catalyst occurs at high temperatures and pressure maintained in the vessel. This method leads to the formation of powders with fine size or narrow size distribution with good chemical homogeneity and is dependent on some reaction parameters such as reaction time, pH value, temperature, solvent, etc. Surfactants also inhibit the growth of crystals by forming an ultrathin structure. Parveen et al. showed the pH dependence of hydrothermal reaction involving coupling of PPy with ZrO_2 photocatalyst [53]. Typically, the ZrO_2/PPy composite was fabricated by maintaining the hydrothermal reaction condition (180 °C/24 h) with the adjustment of pH value. The individual PPy and ZrO_2 system showed the planer-structured PPy nanosheets with spherical ZrO_2 particles. TEM results also revealed the wrinkled lamer structure nanosheets of PPy and ZrO_2 samples (Figure 5a). Besides pH, the hydrothermal temperature also affects the morphology of the particles. As Rashid et al. prepared the ZrO_2 doped $ZnCo_2O_4$ nanocomposites by the hydrothermal process with sulfate as a precursor, ethylene glycol (EG) and water as solvents at 250 to 650 °C calcination temperature [61]. The maximum increase in the surface area of ZrO_2-$ZnCo_2O_4$ was achieved at 350 °C calcined temperature. After calcination, the ZrO_2-$ZnCo_2O_4$ showed the presence of granular particles. Furthermore, the SEM results revealed the appearance of uniform-size nanoparticles of ZrO_2-$ZnCo_2O_4$ composites at higher temperatures (Figure 5b).

4.1.2. Crystal Structure Engineering

The introduction of an impure atom can distort the crystal structure and change the balance of the ZrO_2 photocatalyst by creating the OVs on its surface. Doping with suitable dopants further leads to a change in the morphology of the nanoparticles. For example, Wahba et al. analyzed the variation in morphology of Zr doped ZrO_2/ZnO nanocomposite by preparing it with EG as a complexing agent [22]. The 2.5 wt% of Zr concentration changed the morphology of nanoparticles to elongated non-uniform distribution with large size. By increasing the concentration up to 5 wt%, the particle exhibited uniform

distribution with less agglomeration. Moreover, the SEM results also showed the presence of homogeneous particle size and uniform distribution with 30, 40, and 50 wt% of Zr concentration in ZrO_2/ZnO nanocomposite. In a different study, Navio et al. studied the distinction in the morphology of ZrO_2 photocatalysts by doping with Fe [62]. The Fe/ZrO_2 was prepared by maintaining the appropriate room temperature, and pH (9–10) of the sample. The SEM results revealed that the particles have a large shape and dimension distribution. With increasing the Fe content in the sample, the particles exhibited a high degree of wrinkled texture due to surface deposition. TEM descriptions indicated no substantial change in the morphology of the sample. However, in some cases, enlarged and different round-size grain particles were also observed.

Various studies have been reported to date to study the morphology of ZrO_2 photocatalysts. Agorku et al. prepared the multi-element doped ZrO_2 with Gd, C, N, and S elements to study the morphology of the photocatalyst [63]. The TEM results revealed the presence of a small-size multi-element doped ZrO_2 with spherical shape and distinct grain boundaries. However, the SEM monographs showed uniform morphology with a crystalline-shaped photocatalyst. Furthermore, 0.6% Gd doped C, N, and S-ZrO_2 exhibited the highest photocatalytic activity due to reduced bandgap energy and improved surface-active sites of the photocatalyst as a result of multi-element doping. Chen et al. also studied the morphology of g-C_3N_4 loaded ZrO_{2-x} nanotubes [55]. ZrO_2 nanotubes are tailored through the anodic oxidation of ZrO_2 in a two-electrode system with a 20 mm diameter for each electrode. The prepared ZrO_{2-x} nanotubes were further annealed at 550 °C for 3 h in the presence of Argon. The SEM results showed the clean surface morphology of ZrO_{2-x} nanotubes with a 50 nm diameter. By increasing the g-C_3N_4 concentration, the optimal 0.09CN/ZrO_{2-x} sample exhibited completely covered structure nanotubes. Furthermore, TEM results revealed the regular and clean tubular morphology of ZrO_{2-x} nanotubes whereas the tubular morphology of 0.06 CN/ZrO_{2-x} nanotubes with apparent attachments was further observed by increasing the g-C_3N_4 concentration. The presence of g-C_3N_4 in the composite was confirmed with the help of Fourier transform infrared (FTIR) spectroscopy as delineated in Figure 5c. The broad band of g-C_3N_4 in the NH_2 group stretching mode was observed at 3178 cm^{-1}, while for ZrO_{2-x}, the NTs showed a broad band of OH stretching at 3420 cm^{-1}. The Zr-O bond in ZrO_2 corresponds to 490, 580, and 780 cm^{-1} bands vibrations and the composite showed a peak at 2046 cm^{-1}. The as-synthesized composite exhibited 90.6% degradation of tetracycline hydrochloride after 1 h of visible light exposure.

4.2. Top-Down Strategies

4.2.1. Thermal Treatment

Thermal treatment is a significant method utilized for the introduction of OVs in ZrO_2 at high temperatures, which leads to the cleavage of bonds and further boosts the escape of atoms from the lattice. At definite temperatures, the metals become decomposed to form nanoparticles by involving a chemical reaction. For instance, Zhang et al. prepared an S-scheme g-C_3N_4/ZrO_2 heterostructure via a simple calcination method [26]. Experimental results explained the morphology changes in g-C_3N_4/ZrO_2 heterojunction after variation in calcination temperature. The presence of irregularly arranged nanoparticles on the surface of ZrO_2 with the variation in calcination temperature was confirmed by SEM results. With variation in the g-C_3N_4 concentration, the surface of ZrO_2 photocatalyst became dimmer by the existence of spindle-shaped nanoparticles. It has been observed that the mixing of two metal oxide phases can also help to modulate the photocatalytic activity by inhibiting the crystal growth during the heterostructure formation via calcination. For instance, the heterojunction formation between ZrO_2 and Bi_2O_3 via post-thermal treatment rendered a facile morphology control approach by inhibiting the crystal growth of Bi_2O_3 [64]. From the TEM images, an optimal particle size of 20 nm was observed and was in good agreement with the XRD results. The UV-Visible diffuse reflectance spectroscopy (UV-vis-DRS) spectra of Bi_2O_3-ZrO_2, Bi_2O_3, and ZrO_2 were depicted in Figure 5d where a red shift in the

composite was observed due to the electron–electron transition in between bare ZrO_2 and Bi_2O_3. The spectra also explained the absorbance intensity shift of Bi_2O_3-ZrO_2 towards the longer wavelength than Bi_2O_3 and ZrO_2. Hence, thermal treatment can be successfully employed to modulate the surface morphology of ZrO_2 and ZrO_2-based photocatalysts.

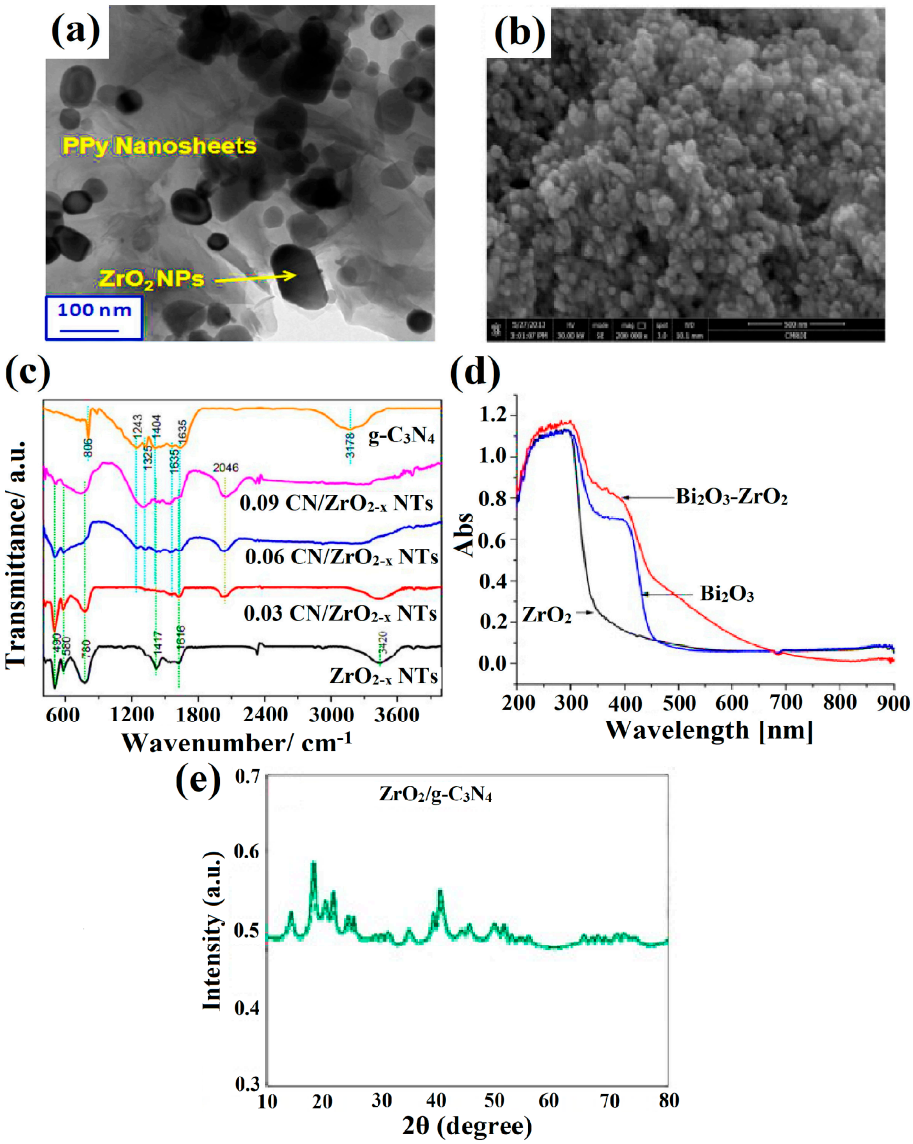

Figure 5. (**a**) HRTEM images and SAED pattern of ZrO_2/ PPy composite, reproduced with permission from Elsevier (License NO. 5333050908229) [53], (**b**) SEM images of calcined ZrO_2-$ZnCo_2O_4$ at 650 °C, reprinted with permission from Elsevier (License NO. 5333051169811) [61], (**c**) FTIR spectrum of g-C_3N_4, ZrO_2 NTs and g-C_3N_4/ZrO_{2-x} NTs, reprinted with permission from Elsevier (License NO. 5332980412880) [55], (**d**) UV-vis-DRS spectrum of Bi_2O_3-ZrO_2, Bi_2O_3, and ZrO_2, reproduced with permission from Elsevier (License NO. 5333060789631) [64], and (**e**) XRD pattern of 30 wt% ZrO_2/g-C_3N_4 [65].

4.2.2. Ultrasonication

Sonication involves the dispersion of the precursor in a solvent followed by further exfoliation of materials. Furthermore, shock waves and high-speed inter-particle collisions also help to improve the surface structure and may sometimes induce the formation of OVs. Zarei et al. synthesized ZrO_2/g-C_3N_4 heterojunction via mixing of g-C_3N_4 powder into ZrO_2 colloidal dispersion through ultrasonic treatment at 30 °C for 2 h [65]. The integration of ZrO_2 nanoparticles into g-C_3N_4 increased their surface area to 51.8 m^2 g^{-1} due to its

distinct morphology. The TEM results indicated that g-C_3N_4 showed planer and sheet-like structures while ZrO_2 nanoparticles were spherical in shape with a 15 nm particle size. Additionally, the XRD pattern revealed the existence of strong and sharp diffraction peaks, which confirmed a high degree of crystallinity in the sample (Figure 5e). Furthermore, the incorporation of ultrasonic treatment with various dopant concentrations can also disturb the morphology of the ZrO_2 photocatalyst. For example, Yu et al. synthesized the TiO_2-N/$ZrO_{2-x}N_x$ heterojunction by subjecting the precursors such as $ZrOCl_2 \cdot 8H_2O$ and Ti $(OC_4H_9)_4$ under ultrasonic treatment [46]. With the variation in the concentration of N, the transformation of tetragonal ZrO_2 to monoclinic was strictly inhibited with resultantly improved surface-active sites. The XRD patterns helped to understand the interactions between N atoms with O atoms in ZrO_2 which led to the substitution of O by nitrogen dopants due to high-energy ultrasonic waves.

4.2.3. Chemical Reduction

Chemical reduction is a method used for the reduction of ionic salt in the presence of surfactants by using reducing agents such as sodium borohydride, lithium aluminum hydride, etc. Interestingly, OVs can also be introduced with the help of reducing agents and by varying the concentration of reductants, the content of vacancies can be controlled. For instance, Qin et al. produced a B@ZrO_2-OV photocatalyst through the introduction of $NaBH_4$ as reducing agent [28]. In this process, ZrO_2 and $NaBH_4$ were taken in different weight ratios and heated at 650 °C for 2 h followed by the annealing of the sample. More importantly, the weight ratios of ZrO_2:$NaBH_4$ was optimized to 1:0.4 because, beyond this, a further increase in the amount of $NaBH_4$ meant that the crystal phase of ZrO_2 was transformed into ZrB_2. The electron paramagnetic resonance (EPR) spectroscopy confirmed the existence of OVs in the B@ZrO_2 photocatalyst at 2.003 g-value. Moreover, the XPS analysis showed three deconvoluted peaks at 529.9 eV, 531.4 eV, and 532.8 eV ascribed to the lattice oxygen, oxygen deficient, and chemically adsorbed oxygen species, respectively.

5. Photodegradation and Mechanism

Environmental contamination by organic dyes, pharmaceuticals, and insecticides is posing a serious threat worldwide owing to their toxic, cancerous nature and difficulty in total decomposition causing a shortage in drinking water. Thus far, various traditional procedures, including biological, physical, and chemical methods have been used to remove these pollutants, however the applicability of these technologies is limited due to their high cost, risk of hazardous byproducts, and poor efficiency. As a result, a more direct and effective way to deal with these contaminants is highly essential [55,66]. Water treatment employing a simple method like photocatalysis is in the limelight owing to its low energy requirement, cost-effectiveness, capacity to adsorb a wide range of natural and inorganic substances on the photocatalyst's surface, and complete degradation without hazardous by-products [67]. Even photocatalysis seemed to be a promising method due to the easy availability of a large amount of solar energy [23]. Semiconductor photocatalytic activity has potential applications in the degradation of environmental contaminants and pollutant transformation. Thus, it has aroused a lot of attention [68].

5.1. Organic Pollutant Degradation

Organic pollutants are identified as harmful for human health as they are toxic, carcinogenic, and teratogenic, so the use of heterogeneous photocatalysis to decontaminate wastewater containing organic compounds is an attractive solution to the effluent treatment problem since it brings about chemical degradation into non-toxic molecules like carbon dioxide and water [29,66]. Charge transfer and electron transfer are involved in the degradation of organic pollutants, and these processes are impacted by the presence of charged species [69]. The alluring features of ZrO_2 involving physicochemical stability and distinctive band structures render optimal photodegradation ability, however the broad bandgap and low separation rate of photocarriers limit its wide-scale practical uses [55]. However,

the synergistic coupling of ferrites with zirconia boosts the overall photoactivity by the combined action of inhibited charge separation and integration of photo and Fenton activity. In detail, Figure 6a depicts the suggested photocatalytic process on the $ZrO_2/ZnFe_2O_4$ nanocomposite (ZZFO 12 NC) for the photodegradation of indigo carmine dye (98%) [31]. After the excitation and isolation of photocarriers, the reaction of photoinduced electrons oxygen yielded superoxide radicals ($\bullet O_2^-$), which further reacted with H_2O to produce H_2O_2. This generated H_2O_2 reaction with α-Fe_2O_3 in ZZFO 12 further produced •OH radicals and participated in dye degradation, as shown in Equations (1)–(7)

$$ZZFO + h\nu \rightarrow ZrO_2 - h^+ + ZnFe_2O_4 - e^- \quad (1)$$

$$ZnFe_2O_4 - e^- + O_2^{\bullet} \rightarrow \bullet O_2^- \quad (2)$$

$$\bullet O_2^- + H_2O \rightarrow H_2O_2 + \bullet OH \quad (3)$$

$$H_2O_2 + \alpha - Fe_2O_3 \rightarrow 2\,\bullet OH \quad (4)$$

$$h^+ + OH^- \rightarrow 2\,\bullet OH \quad (5)$$

$$\bullet OH + \text{indigo carmine} \rightarrow \text{Degradation} \quad (6)$$

$$\bullet O_2^- + \text{indigo carmine} \rightarrow \text{Degradation} \quad (7)$$

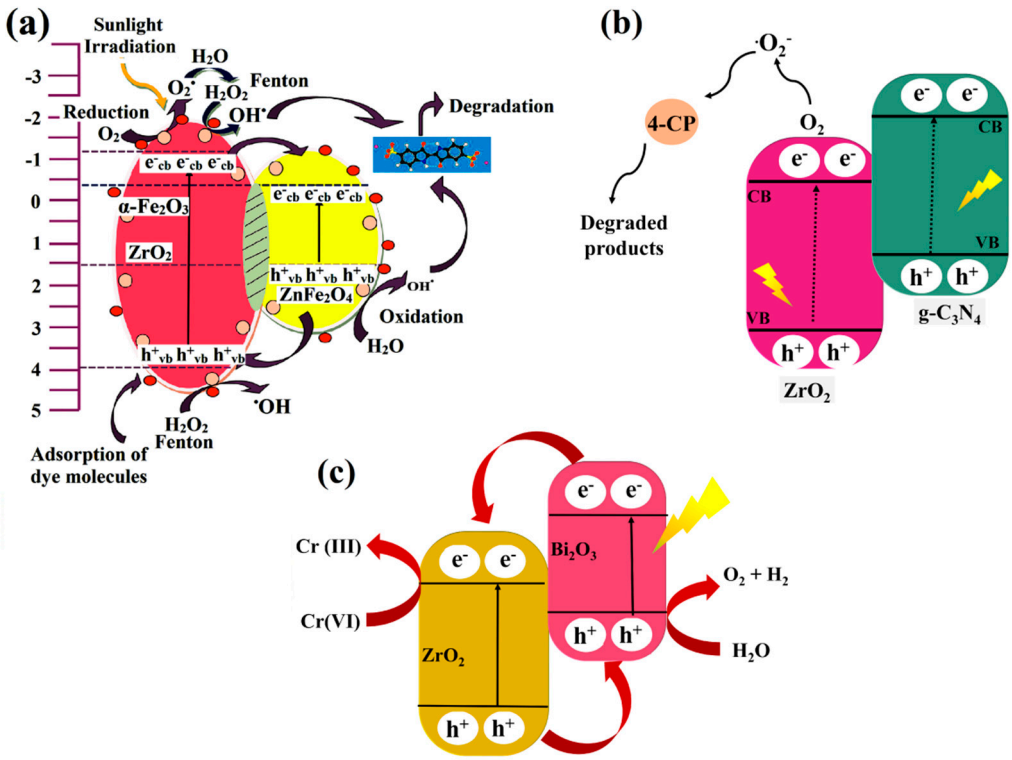

Figure 6. (**a**) Photodegradation pathway of indigo carmine dye under sunlight exposure for $ZrO_2/ZnFe_2O_4$ composite, reprinted with permission from Elsevier (License NO. 5333060926293) [31], (**b**) schematic representation of charge carriers' separation on 30 wt% ZrO_2/g-C_3N_4 composites under light illumination [65], and (**c**) systematic presentation of photocarriers transfer in Bi_2O_3-ZrO_2 hybrid in presence of visible light, reproduced with permission from Elsevier (License NO. 5333060789631) [64].

Other than dyes, phenolic compounds have also been treated effectively with ZrO_2-based nanocomposites. For example, ZrO_2/g-C_3N_4 nanocomposite synthesized by ultrasonication method for the efficient degradation of 4-chlorophenol (4-CP) (Figure 6b) in water with the highest degradation rate of 0.0173 min^{-1} [65]. The synergistic action of higher surface area with exposed active sites facilitates the adsorption of 4-CP and the surface-induced

charges accelerated the formation of $\bullet O_2^-$ radicals which boosted the degradation efficiency. Moreover, from the radical scavenging results, it was confirmed that $\bullet O_2^-$ radicals and h+ primarily participated in the degradation process.

5.2. Inorganic Pollutant Degradation

The higher concentration of inorganic pollutants in the water due to their discharge from various industries like fertilizers, refineries, and pharmaceuticals is causing a major threat to human as well as aquatic lives. Thus the photocatalytic treatment of such toxic effluents using ZrO_2 as a photocatalyst can be a potential solution. In this regard, enhancement in Cr (VI) photoreduction under visible light irradiation is achieved by developing a Bi_2O_3-ZrO_2 nanocomposite [64]. Bi_2O_3-ZrO_2 has a greater photocatalytic activity (92.30%) after an irradiation period of 180 min. The mechanism for enhanced photocatalytic activity of Bi_2O_3-ZrO_2 is explained according to previously published literature on the photocatalytic activity of nanocomposites. Typically, Cr (VI) is photo-reduced by CB electrons captured by ZrO_2, and the VB holes further oxidized H_2O to create O_2 (Figure 6c). The detailed photocatalytic processes that occur on the surface of Bi_2O_3-ZrO_2 are summarized in Equations (8)–(11):

$$Bi_2O_3 + hv \rightarrow Bi_2O_3\left(h_{VB}^+ + e_{CB}^-\right) \quad (8)$$

$$Bi_2O_3\left(e_{CB}^-\right) + ZrO_2 \rightarrow Bi_2O_3 + ZrO_2\left(e_{CB}^-\right) \quad (9)$$

$$ZrO_2\left(6e_{CB}^-\right) + Cr_2O_7^{2-} + 14H^+ \rightarrow 2Cr^{3+} + 7H_2O + ZrO_2 \quad (10)$$

$$2H_2O + 4h^+ \rightarrow O_2 + 4H^+ \quad (11)$$

Various ZrO_2-based semiconductor photocatalysts with incremented photodegradation activity are summarized in Table 1 [59,70–79].

Table 1. Summary of various ZrO_2-based semiconductor photocatalysts for the incremented photocatalytic degradation of aqueous phase pollutants.

Photocatalyst	Enhancement Strategies	Reaction Parameter	Targeted Pollutant	Photocatalyst Efficiency	Ref.
Ni doped ZrO_2	Doping	Visible light lamp (>400 nm), 15 mg photocatalyst	Methylene blue	90.2% in 100 min.	[59]
C-doped ZrO_2	Doping	PL-L lamp, 0.2 g/L photocatalyst	Methylene blue	75%	[70]
Nd doped ZrO_2	Doping	pH = 7	Methylene blue, Rhodamine B, and acetophenone	90%, 77%, and 60%	[71]
Al_2O_3/ZrO_2	Heterojunction	Visible light, 0.04 g catalyst	Reactive blue 222 and Reactive yellow 145	91.4% and 94.6% in 60 min.	[72]
RE/ZrO_2 (RE = Sm, Eu)	Heterojunction	350 W Xenon lamp	Methylene blue and Rhodamine B	100% in 30 min. and 96.3% in 90 min.	[73]
ZnO QDs@ZrO_2-TiO_2	Heterojunction	Ultra violet light	Congo Red	94.62%	[74]
ZrO_2/Dy_2O_3	Heterojunction	Xenon lamp with cut-off UV filter	Rhodamine B, and Methylene blue	100% in 30 min. and 87.79%	[75]
TiO_2-ZrO_2	Heterojunction	125 W Mercury lamp, pH = 7.6, 10 mg/L photocatalyst	Metformin	92% in 150 min.	[76]
g-C_3N_4/ZrO_2	Heterojunction	50 W LED lamp, 30 mg photocatalyst	Methylene blue, Rhodamine B, Congo Red, and Tetracycline	96%, 98%, 90%, and 83%	[77]
$CuCo_2O_4$@ZrO_2	Heterojunction	Visible light	Tetracycline	95%	[78]
TiO_2/ZrO_2	Heterojunction	100 W LED lamp	Rhodamine B	90%	[79]

6. Concluding Remarks

Among various metal-oxide photocatalysts, ZrO_2 is an n-type wide bandgap semiconducting material with substantial features like physicochemical stability, facile synthesis, cost-effectiveness, etc. In spite of various fascinating properties of ZrO_2, there are various factors that limit its practical applications. Therefore, to enhance its photocatalytic activity, suitable modification techniques such as doping, heterojunction formation, and vacancy creations have been opted. Considering that, the present study highlights the recent advances in the photocatalytic activity of ZrO_2 and its nanocomposites. The structural features, formation of band edge potentials, and the characteristics of optical as well as electronic properties are comprehensively discussed by integrating experimental and computational studies. Various strategic modulations, such as morphology and structural control, bandgap engineering, heterostructure construction, and vacancy engineering are the major approaches for synergistically improving the charge carrier's dynamics and light harvesting ability of ZrO_2. Moreover, various synthetic routes involving bottom-up and top-down methods can be utilized to modulate the physicochemical features of ZrO_2 and attain effective photocatalytic degradation performance. Thus, it is envisaged that, with the aid of the research advances discussed in this review, future research can be focused to explore the photocatalytic performance of modified ZrO_2 for large-scale photocatalytic applications.

Author Contributions: Writing—original draft preparation, V.R. and A.S. (Amit Sharma); writing—review and editing, P.S. and A.K.; visualization and project administration, P.S., S.T. and A.S. (Archana Singh); conceptualization, validation and supervision, Q.V.L., V.H.N. and P.R. All authors have read and agreed to the published version of the manuscript.

Funding: This research received no external funding.

Data Availability Statement: Not applicable.

Conflicts of Interest: The authors declare no conflict of interest.

References

1. Hosseini-Bandegharaei, A. Adsorption and photocatalysis compiled toxic dyes mineralization using graphitic carbon nitride modified $ZnFe_2O_4$ and $CoFe_2O_4$ photocatalysts supported onto N-doped graphene. *Desalination Water Treat* **2020**, *191*, 381–399.
2. Kumar, A.; Raizada, P.; Hosseini-Bandegharaei, A.; Thakur, V.K.; Nguyen, V.H.; Singh, P. C-, N-Vacancy defect engineered polymeric carbon nitride towards photocatalysis: Viewpoints and challenges. *J. Mater. Chem. A* **2021**, *9*, 111–153. [CrossRef]
3. Pirhashemi, M.; Habibi-Yangjeh, A.; Pouran, S.R. Review on the criteria anticipated for the fabrication of highly efficient ZnO-based visible-light-driven photocatalysts. *J. Ind. Eng. Chem.* **2018**, *62*, 1–25. [CrossRef]
4. Kumari, P.; Bahadur, N.; Kong, L.; O'Dell, L.A.; Merenda, A.; Dumee, L. Engineering Schottky-like and heterojunction material for enhanced photocatalysis performance-a review. *Adv. Mater.* **2022**, *3*, 2309–2323. [CrossRef]
5. Almeida, F.; Grzebielucka, E.C.; Antunes, S.R.M.; Borges, C.P.F.; Andrade, A.V.C.; Souza, É.C.F. Visible light activated magnetic photocatalysts for water treatment. *J. Environ. Manag.* **2020**, *273*, 111143. [CrossRef] [PubMed]
6. Alshorifi, F.T.; Ali, S.L.; Salama, R.S. Promotional Synergistic Effect of Cs–Au NPs on the Performance of Cs–Au/$MgFe_2O_4$ Catalysts in Catalysis 3, 4-Dihydropyrimidin-2 (1H)-Ones and Degradation of RhB Dye. *J. Inorg. Organomet. Polym. Mater.* **2022**, *32*, 3765–3776. [CrossRef]
7. Ahamad, T.; Naushad, M.; Ubaidullah, M.; Alshehri, S. Fabrication of highly porous polymeric nanocomposite for the removal of radioactive U (VI) and Eu (III) ions from aqueous solution. *Polym. J.* **2020**, *12*, 2940. [CrossRef]
8. Balakrishnan, T.; Kiran, K.U.V.; Kumar, S.M.; Raju, A.; Kumar, S.A.; Mayavan, S. Copper particles decorated boron carbon nitride, an efficient catalyst for methyl orange oxidation under sonication and sunlight irradiation. *J. Environ. Chem. Eng.* **2017**, *5*, 564–571. [CrossRef]
9. Alshorifi, F.T.; Alswat, A.A.; Salama, R.S. Gold-selenide quantum dots supported onto cesium ferrite nanocomposites for the efficient degradation of rhodamine B. *Heliyon* **2022**, *8*, e09652. [CrossRef]
10. Al-Enizi, A.M.; Ubaidullah, M.; Ahmed, J.; Ahamad, T.; Ahmad, T.; Shaikh, S.F.; Naushad, M. Synthesis of NiOx@ NPC composite for high-performance supercapacitor via waste PET plastic-derived Ni-MOF. *Compos. B. Eng.* **2020**, *183*, 107655. [CrossRef]
11. Hasija, V.; Raizada, P.; Sudhaik, A.; Sharma, K.; Kumar, A.; Singh, P.; Jonnalagadda, S.B.; Thakur, V.K. Recent advances in noble metal free doped graphitic carbon nitride based nanohybrids for photocatalysis of organic contaminants in water: A review. *Appl. Mater. Today* **2019**, *15*, 494–524. [CrossRef]

12. El-Hakam, S.A.; ALShorifi, F.T.; Salama, R.S.; Gamal, S.; El-Yazeed, W.A.; Ibrahim, A.A.; Ahmed, A.I. Application of nanostructured mesoporous silica/bismuth vanadate composite catalysts for the degradation of methylene blue and brilliant green. *J. Mater. Res. Technol.* **2022**, *18*, 1963–1976. [CrossRef]
13. Thakur, N.; Kumar, K.; Thakur, V.K.; Soni, S.; Kumar, A.; Samant, S.S. Antibacterial and photocatalytic activity of undoped and (Ag, Fe) co-doped CuO nanoparticles via microwave-assisted method. *Nanofabrication* **2022**, *7*. [CrossRef]
14. Andreozzi, R.; Caprio, V.; Insola, A.; Marotta, R. Advanced oxidation processes (AOP) for water purification and recovery. *Catal. Today* **1999**, *53*, 51–59. [CrossRef]
15. Jangwan, J.; Kumar, S.S.; Kumar, V.; Kumar, A.; Kumar, D. A review on the capability of zinc oxide and iron oxides nanomaterials, as a water decontaminating agent: Adsorption and photocatalysis. *Appl. Water Sci.* **2022**, *12*, 1–14.
16. Hussain, N.; Bilal, M.; Iqbal, H.M. Carbon-based nanomaterials with multipurpose attributes for water treatment: Greening the 21st-century nanostructure materials deployment. *Biomater. Polym. Horiz.* **2022**, *1*, 1–11. [CrossRef]
17. Pournemati, K.; Habibi-Yangjeh, A.; Khataee, A. Rational design of $TiO_2/MnMoO_4/MoO_3$ nanocomposites: Visible-light-promoted photocatalysts for decomposition of tetracycline with tandem nn heterojunctions. *Colloids Surf. A Physicochem. Eng. Asp.* **2022**, *655*, 130315. [CrossRef]
18. Pelosato, R.; Bolognino, I.; Fontana, F.; Sora, I.N. Applications of Heterogeneous Photocatalysis to the Degradation of Oxytetracycline in Water: A Review. *Molecules* **2022**, *27*, 2743. [CrossRef]
19. Murillo-Sierra, J.; Hernández-Ramírez, A.; Hinojosa-Reyes, L.; Guzmán-Mar, J. A review on the development of visible light-responsive WO_3-based photocatalysts for environmental applications. *Adv. Chem. Eng.* **2021**, *5*, 100070. [CrossRef]
20. Luo, S.; Zhang, C.; Almatrafi, E.; Yan, M.; Liu, Y.; Fu, Y.; Wang, Z.; Li, L.; Zhou, C.; Xu, P. Photocatalytic water purification with graphitic C_3N_4-based composites: Enhancement, mechanisms, and performance. *Appl. Mater. Today* **2021**, *24*, 101118. [CrossRef]
21. Sang, Y.; Liu, H.; Umar, A. Photocatalysis from UV/Vis to near-infrared light: Towards full solar-light spectrum activity. *ChemCatChem* **2015**, *7*, 559–573. [CrossRef]
22. Wahba, M.A.; Yakout, S.M.; Mohamed, W.A.; Galal, H.R. Remarkable photocatalytic activity of Zr doped ZnO and ZrO_2/ZnO nanocomposites: Structural, morphological and photoluminescence properties. *Mater. Chem. Phys.* **2020**, *256*, 123754. [CrossRef]
23. Pirzada, B.M.; Mir, N.A.; Qutub, N.; Mehraj, O.; Sabir, S.; Muneer, M. Synthesis, characterization and optimization of photocatalytic activity of TiO_2/ZrO_2 nanocomposite heterostructures. *Mater. Sci. Eng. B* **2015**, *193*, 137–145. [CrossRef]
24. Aldeen, E.S.; Jalil, A.A.; Mim, R.S.; Alhebshi, A.; Hassan, N.S.; Saravanan, R. Altered zirconium dioxide based photocatalyst for enhancement of organic pollutants degradation: A review. *Chemosphere* **2022**, *304*, 135349. [CrossRef]
25. Ahmed, W.; Iqbal, J. Co doped ZrO_2 nanoparticles: An efficient visible light triggered photocatalyst with enhanced structural, optical and dielectric characteristics. *Ceram. Int.* **2020**, *46*, 25833–25844. [CrossRef]
26. Zhang, K.; Zhou, M.; Yu, C.; Yang, K.; Li, X.; Dai, W.; Guan, J.; Shu, Q.; Huang, W. Construction of S-scheme g-C_3N_4/ZrO_2 heterostructures for enhancing photocatalytic disposals of pollutants and electrocatalytic hydrogen evolution. *Dyes Pigm.* **2020**, *180*, 108525. [CrossRef]
27. García-López, E.; Marcì, G.; Pomilla, F.; Paganini, M.; Gionco, C.; Giamello, E.; Palmisano, L. ZrO_2 Based materials as photocatalysts for 2-propanol oxidation by using UV and solar light irradiation and tests for CO_2 reduction. *Catal. Today* **2018**, *313*, 100–105. [CrossRef]
28. Qin, Y.; Ding, Z.; Guo, W.; Guo, X.; Hou, C.; Jiang, B.-P.; Liu, C.-G.; Shen, X.-C. A full solar light spectrum responsive B@ ZrO_2–OV photocatalyst: A synergistic strategy for visible-to-NIR photon harvesting. *ACS Sustain. Chem. Eng.* **2020**, *8*, 13039–13047. [CrossRef]
29. Wang, Y.; Zhang, Y.; Lu, H.; Chen, Y.; Liu, Z.; Su, S.; Xue, Y.; Yao, J.; Zeng, H. Novel N-doped ZrO_2 with enhanced visible-light photocatalytic activity for hydrogen production and degradation of organic dyes. *RSC Adv.* **2018**, *8*, 6752–6758. [CrossRef]
30. Kaviyarasu, K.; Kotsedi, L.; Simo, A.; Fuku, X.; Mola, G.T.; Kennedy, J.; Maaza, M. Photocatalytic activity of ZrO_2 doped lead dioxide nanocomposites: Investigation of structural and optical microscopy of RhB organic dye. *Appl. Surf. Sci.* **2017**, *421*, 234–239. [CrossRef]
31. Renuka, L.; Anantharaju, K.; Vidya, Y.; Nagabhushana, H.; Uma, B.; Malini, S.; More, S.S.; Koppad, P. Porous network $ZrO_2/ZnFe_2O_4$ nanocomposite with heterojunction towards industrial water purification under sunlight: Enhanced charge separation and elucidation of photo-mechanism. *Ceram. Int.* **2021**, *47*, 14845–14861. [CrossRef]
32. Idrissi, S.; Ziti, S.; Labrim, H.; Bahmad, L. Sulfur doping effect on the electronic properties of zirconium dioxide ZrO_2. *Mater. Sci. Eng. B* **2021**, *270*, 115200. [CrossRef]
33. Faizan, M.; Siddique, M.N.; Ahmad, S.; Tripathi, P.; Riyajuddin, S. Tunable luminescence in Ce^{3+}/Mn^{2+} co-doped ZrO_2 nanophosphor integrated with theoretical studies on possible (ZrO_2) n clusters using DFT method. *J. Alloys Compd.* **2021**, *853*, 157378. [CrossRef]
34. Zhou, H.; Yao, P.; Gong, T.; Xiao, Y.; Zhang, Z.; Zhao, L.; Fan, K.; Deng, M. Effects of ZrO_2 crystal structure on the tribological properties of copper metal matrix composites. *Tribol. Int.* **2019**, *138*, 380–391. [CrossRef]
35. Lamas, D.; Rosso, A.; Anzorena, M.S.; Fernández, A.; Bellino, M.; Cabezas, M.; de Reca, N.W.; Craievich, A. Crystal structure of pure ZrO_2 nanopowders. *Scr. Mater.* **2006**, *55*, 553–556. [CrossRef]
36. McCullough, J.T.; Trueblood, K. The crystal structure of baddeleyite (monoclinic ZrO_2). *Acta Crystallogr.* **1959**, *12*, 507–511. [CrossRef]

37. Singh, H.; Yadav, K.K.; Bajpai, V.K.; Jha, M. Tuning the bandgap of m-ZrO_2 by incorporation of copper nanoparticles into visible region for the treatment of organic pollutants. *Mater. Res. Bull.* **2020**, *123*, 110698. [CrossRef]
38. Teufer, G. The crystal structure of tetragonal ZrO_2. *Acta Crystallogr.* **1962**, *15*, 1187. [CrossRef]
39. Lin, Y.-F.; Liang, F.-L. ZrO_2/carbon aerogel composites: A study on the effect of the crystal ZrO_2 structure on cationic dye adsorption. *J. Taiwan Inst. Chem. Eng.* **2016**, *65*, 78–82. [CrossRef]
40. Morinaga, M.; Adachi, H.; Tsukada, M. Electronic structure and phase stability of ZrO_2. *J. Phys. Chem. Solids* **1983**, *44*, 301–306. [CrossRef]
41. Koe, W.S.; Lee, J.W.; Chong, W.C.; Pang, Y.L.; Sim, L.C. An overview of photocatalytic degradation: Photocatalysts, mechanisms, and development of photocatalytic membrane. *Environ. Sci. Pollut. Res.* **2020**, *27*, 2522–2565. [CrossRef] [PubMed]
42. Wang, J.; Huang, J.; Meng, J.; Li, Q.; Yang, J. Double-hole codoped huge-gap semiconductor ZrO_2 for visible-light photocatalysis. *Phys. Chem. Chem. Phys.* **2016**, *18*, 17517–17524. [CrossRef] [PubMed]
43. Mazumder, J.T.; Mayengbam, R.; Tripathy, S. Theoretical investigation on structural, electronic, optical and elastic properties of TiO_2, SnO_2, ZrO_2 and HfO_2 using SCAN meta-GGA functional: A DFT study. *Mater. Chem. Phys.* **2020**, *254*, 123474. [CrossRef]
44. Yang, R.; Zhang, Y.; Fan, Y.; Wang, R.; Zhu, R.; Tang, Y.; Yin, Z.; Zeng, Z. $InVO_4$-based photocatalysts for energy and environmental applications. *Chem. Eng.* **2022**, *428*, 131145. [CrossRef]
45. Renuka, L.; Anantharaju, K.; Sharma, S.; Nagaswarupa, H.; Prashantha, S.; Nagabhushana, H.; Vidya, Y. Hollow microspheres Mg-doped ZrO_2 nanoparticles: Green assisted synthesis and applications in photocatalysis and photoluminescence. *J. Alloys Compd.* **2016**, *672*, 609–622. [CrossRef]
46. Yu, Y.; Zhang, P.; Kuang, Y.; Ding, Y.; Yao, J.; Xu, J.; Cao, Y. Adjustment and Control of Energy Levels for TiO_2–N/$ZrO_{2-x}N_x$ with Enhanced Visible Light Photocatalytic Activity. *J. Phys. Chem. C* **2014**, *118*, 20982–20988. [CrossRef]
47. Xia, Y.; Sun, Q.; Wang, D.; Zeng, X.-F.; Wang, J.-X.; Chen, J.-F. Surfactant-free aqueous dispersions of shape-and size-controlled zirconia colloidal nanocrystal clusters with enhanced photocatalytic activity. *Langmuir* **2019**, *35*, 11755–11763. [CrossRef]
48. Fu, X.; Clark, L.A.; Yang, Q.; Anderson, M.A. Enhanced photocatalytic performance of titania-based binary metal oxides: TiO_2/SiO_2 and TiO_2/ZrO_2. *Environ. Sci. Technol.* **1996**, *30*, 647–653. [CrossRef]
49. Linnik, O.; Shestopal, N.; Smirnova, N.; Eremenko, A.; Korduban, O.; Kandyba, V.; Kryshchuk, T.; Socol, G.; Stefan, N.; Popescu-Pelin, G. Correlation between electronic structure and photocatalytic properties of non-metal doped TiO_2/ZrO_2 thin films obtained by pulsed laser deposition method. *Vacuum* **2015**, *114*, 166–171. [CrossRef]
50. Berlin, I.J.; Joy, K. Optical enhancement of Au doped ZrO_2 thin films by sol–gel dip coating method. *Physica B Condens. Matter* **2015**, *457*, 182–187. [CrossRef]
51. Anwer, H.; Park, J.-W. Synthesis and characterization of a heterojunction rGO/ZrO_2/Ag_3PO_4 nanocomposite for degradation of organic contaminants. *J. Hazard. Mater.* **2018**, *358*, 416–426. [CrossRef] [PubMed]
52. Gurushantha, K.; Renuka, L.; Anantharaju, K.; Vidya, Y.; Nagaswarupa, H.; Prashantha, S.; Nagabhushana, H. Photocatalytic and photoluminescence studies of ZrO_2/ZnO nanocomposite for LED and waste water treatment applications. *Mater. Today Proc.* **2017**, *4*, 11747–11755. [CrossRef]
53. Parveen, A.; Surumbarkuzhali, N. Spatial separation of photo-generated carriers and enhanced photocatalytic performance on ZrO2 catalysts via coupling with PPy. *Inorg. Chem. Commun.* **2020**, *120*, 108153. [CrossRef]
54. Habibi-Yangjeh, A.; Basharnavaz, H. Ni/P, Pt/P and Pd/P-modified graphitic carbon nitride nanosheets for hydrogen storage application using a DFT investigation. *Mol. Phy.* **2022**, e2124934. [CrossRef]
55. Chen, Q.; Yang, W.; Zhu, J.; Fu, L.; Li, D.; Zhou, L. Enhanced visible light photocatalytic activity of g-C_3N_4 decorated ZrO_{2-x} nanotubes heterostructure for degradation of tetracycline hydrochloride. *J. Hazard. Mater.* **2020**, *384*, 121275. [CrossRef]
56. Hao, Y.; Li, L.; Liu, D.; Yu, H.; Zhou, Q. The synergy of SPR effect and Z-scheme of Ag on enhanced photocatalytic performance of 3DOM Ag/CeO_2-ZrO_2 composite. *J. Mol. Catal.* **2018**, *447*, 37–46. [CrossRef]
57. Xu, Q.; Zhang, L.; Cheng, B.; Fan, J.; Yu, J. S-scheme heterojunction photocatalyst. *Chem* **2020**, *6*, 1543–1559. [CrossRef]
58. Sobolev, A.; Varaksin, A.; Keda, O.; Khaimenov, A. Electronic structure and charge state of oxygen vacancies in perfect ZrO_2 crystals. *Phys. Status Solidi B Basic Res.* **1990**, *162*, 165–171. [CrossRef]
59. Reddy, C.V.; Reddy, I.N.; Ravindranadh, K.; Reddy, K.R.; Kim, D.; Shim, J. Ni-dopant concentration effect of ZrO_2 photocatalyst on photoelectrochemical water splitting and efficient removal of toxic organic pollutants. *Sep. Purif. Technol.* **2020**, *252*, 117352. [CrossRef]
60. Ma, H.; He, Y.; Chen, P.; Wang, H.; Sun, Y.; Li, J.; Dong, F.; Xie, G.; Sheng, J. Ultrathin Two-Dimensional Bi-Based photocatalysts: Synthetic strategies, surface defects, and reaction mechanisms. *Chem. Eng. J.* **2021**, *417*, 129305. [CrossRef]
61. Rashid, J.; Barakat, M.; Mohamed, R.; Ibrahim, I. Enhancement of photocatalytic activity of zinc/cobalt spinel oxides by doping with ZrO_2 for visible light photocatalytic degradation of 2-chlorophenol in wastewater. *J. Photochem. Photobiol.* **2014**, *284*, 1–7. [CrossRef]
62. Navio, J.; Hidalgo, M.; Colon, G.; Botta, S.; Litter, M. Preparation and physicochemical properties of ZrO_2 and Fe/ZrO_2 prepared by a sol− gel technique. *Langmuir* **2001**, *17*, 202–210. [CrossRef]
63. Agorku, E.; Pandey, A.; Mamba, B.; Mishra, A. Gd, C, N, S multi-doped ZrO_2 for photocatalytic degradation of indigo carmine dye from synthetic water under simulated solar light. *Mater. Today Proc.* **2015**, *2*, 3909–3920. [CrossRef]
64. Vignesh, K.; Priyanka, R.; Rajarajan, M.; Suganthi, A. Photoreduction of Cr (VI) in water using Bi_2O_3–ZrO_2 nanocomposite under visible light irradiation. *J. Mater. Sci. Eng. B* **2013**, *178*, 149–157. [CrossRef]

65. Zarei, M. Ultrasonic-assisted preparation of ZrO_2/g-C_3N_4 nanocomposites with high visible-light photocatalytic activity for degradation of 4-chlorophenol in water. *Water-Energy Nexus* **2020**, *3*, 135–142. [CrossRef]
66. Zhao, W.; Adeel, M.; Zhang, P.; Zhou, P.; Huang, L.; Zhao, Y.; Ahmad, M.A.; Shakoor, N.; Lou, B.; Jiang, Y.; et al. A critical review on surface modified nano-catalysts application for photocatalytic degradation of volatile organic compounds. *Environ. Sci. Nano* **2022**, *9*, 61–80. [CrossRef]
67. Xu, F.; Lai, C.; Zhang, M.; Li, B.; Liu, S.; Chen, M.; Li, L.; Xu, Y.; Qin, L.; Fu, Y. Facile one-pot synthesis of carbon self-doped graphitic carbon nitride loaded with ultra-low ceric dioxide for high-efficiency environmental photocatalysis: Organic pollutants degradation and hexavalent chromium reduction. *J. Colloid Interface Sci.* **2021**, *601*, 196–208. [CrossRef]
68. Zheng, H.; Liu, K.; Cao, H.; Zhang, X. L-Lysine-assisted synthesis of ZrO_2 nanocrystals and their application in photocatalysis. *J. Phys. Chem. C* **2009**, *113*, 18259–18263. [CrossRef]
69. Polisetti, S.; Deshpande, P.A.; Madras, G. Photocatalytic activity of combustion synthesized ZrO_2 and ZrO_2–TiO_2 mixed oxides. *Ind. Eng. Chem. Res.* **2011**, *50*, 12915–12924. [CrossRef]
70. de Moraes, N.P.; de Azeredo, C.A.S.H.; Bacetto, L.A.; da Silva, M.L.C.P.; Rodrigues, L.A. The effect of C-doping on the properties and photocatalytic activity of ZrO_2 prepared via sol-gel route. *Optik* **2018**, *165*, 302–309. [CrossRef]
71. Keerthana, S.P.; Yuvakkumar, R.; Kumar, P.S.; Ravi, G.; Velauthapillai, D. Nd doped ZrO_2 photocatalyst for organic pollutants degradation in wastewater. *Environ. Technol. Innov.* **2022**, *28*, 102851. [CrossRef]
72. Yaghoubi, A.; Ramazani, A.; Taghavi Fardood, S. Synthesis of Al_2O_3/ZrO_2 nanocomposite and the study of its effects on photocatalytic degradation of reactive blue 222 and reactive yellow 145 dyes. *ChemistrySelect* **2020**, *5*, 9966–9973. [CrossRef]
73. Du, W.; Zhu, Z.; Zhang, X.; Wang, D.; Liu, D.; Qian, X.; Du, J. RE/ZrO_2 (RE= Sm, Eu) composite oxide nano-materials: Synthesis and applications in photocatalysis. *Mater. Res. Bull.* **2013**, *48*, 3735–3742. [CrossRef]
74. Zhou, Q.; Li, L.; Zhang, X.; Yang, H.; Cheng, Y.; Che, H.; Wang, L.; Cao, Y. Construction of heterojunction and homojunction to improve the photocatalytic performance of ZnO quantum dots sensitization three-dimensional ordered hollow sphere ZrO_2–TiO_2 arrays. *Int. J. Hydrog. Energy* **2020**, *45*, 31812–31824. [CrossRef]
75. Du, W.; Wang, X.; Li, H.; Ma, D.; Hou, S.; Zhang, J.; Qian, X.; Pang, H. ZrO_2/Dy_2O_3 Solid Solution Nano-Materials: Tunable Composition, Visible light–Responsive Photocatalytic Activities and Reaction Mechanism. *J. Am. Ceram. Soc.* **2013**, *96*, 2979–2986. [CrossRef]
76. Carbuloni, C.F.; Savoia, J.E.; Santos, J.S.; Pereira, C.A.; Marques, R.G.; Ribeiro, V.A.; Ferrari, A.M. Degradation of metformin in water by TiO_2–ZrO_2 photocatalysis. *J. Environ. Manag.* **2020**, *262*, 110347. [CrossRef]
77. Tanzifi, M.; Jahanshahi, M.; Peyravi, M.; Khalili, S. A morphological decoration of g-C_3N_4/ZrO_2 heterojunctions as a visible light activated photocatalyst for degradation of various organic pollutants. *J. Environ. Chem. Eng.* **2022**, *10*, 108600. [CrossRef]
78. Alotaibi, M.R.; Mahmoud, M.H.H. Promptness of tetracycline pollutant degradation via $CuCo_2O_4$@ZrO_2 nanocomposites photocatalyst. *Opt. Mater.* **2022**, *126*, 112200. [CrossRef]
79. Abdi, J.; Yahyanezhad, M.; Sakhaie, S.; Vossoughi, M.; Alemzadeh, I. Synthesis of porous TiO_2/ZrO_2 photocatalyst derived from zirconium metal organic framework for degradation of organic pollutants under visible light irradiation. *J. Environ. Chem. Eng.* **2019**, *7*, 103096. [CrossRef]